Journal of Geothermal Research and Volcanology (2026) 09-17

Contents lists available at FoundAE

Journal of Geothermal Research and Volcanology

Journal homepage: https://ejournal.foundae.com/index.php/jograv/index

Geophysical constraints on granite related non-volcanic geothermal systems in West Kalimantan, Indonesia

Salsabila Siregar[a,*], Berwyn Dzaky Radhitya[b]

[a] Department of Physics, Institut Teknologi Sumatera, Way Huwi, Jati Agung, South Lampung, Lampung 35365, Indonesia
[b] Faculty of Life and Environmental Sciences, University of Tsukuba, Tsukuba, Ibaraki 305-0006, Japan

ARTICLE INFO

Keywords:
Non-volcanic
geothermal system
Subsurface structure
Lithological control
Granite intrusion
West Kalimantan

ABSTRACT

Geothermal resources are typically concentrated in active volcanic provinces; however, significant geothermal potential also occurs in non-volcanic environments, commonly referred to as non-volcanic geothermal systems. In Indonesia, such systems have been documented in the Riau Archipelago, Bangka Island, Belitung Island, and Kalimantan. This study investigates the subsurface structural and lithological controls of three non-volcanic geothermal prospects in West Kalimantan Province, namely Sape, Sibetuk, and Nanga Dua. Granitic rocks are interpreted as a potential heat source governing reservoir development, although groundwater heating may also be influenced by pressure gradients within sedimentary basins. To constrain the controlling rock units and subsurface geometry, gravity observations were processed and integrated into two-dimensional (2D) and three-dimensional (3D) forward modeling. The results reveal distinct dominant lithologies at each prospect. The Sape geothermal prospect is primarily associated with slate units with an estimated density of 2.6 g/cm³. The Sibetuk prospect is characterized by granitic formations with a comparable density of 2.6 g/cm³, whereas the Nanga Dua prospect is mainly developed within sandstone formations with a density of 2.31 g/cm³. The 2D–3D models consistently indicate that granitic bodies beneath the Melawi–Ketungau Basin represent the most plausible geothermal heat source in the study area. This work provides one of the first integrated gravity-based structural interpretations for non-volcanic geothermal prospects in West Kalimantan. The findings offer a geophysical framework for ranking exploration targets and reducing uncertainty in geothermal resource assessment within sedimentary basin settings.

1. Introduction

Geothermal energy has long been recognized as one of the most reliable renewable energy resources due to its ability to provide stable baseload power with relatively low greenhouse gas emissions. In comparison with intermittent renewable sources such as solar and wind, geothermal energy offers continuous availability and high capacity factors, making it strategically important for national energy security and decarbonization policies [1, 2]. Globally, geothermal utilization has historically been concentrated in tectonically active regions, particularly along plate boundaries and volcanic arcs where elevated heat flow is commonly associated with shallow magmatic systems. In such settings, high-temperature geothermal reservoirs are frequently controlled by volcanic structures, young intrusive bodies, and extensive fracture networks that facilitate fluid circulation. Consequently, most geothermal conceptual models and exploration workflows have been developed primarily for volcanic environments.

Despite this long-standing focus, geothermal resources are not exclusive to volcanic regions. Over the past decades, geothermal exploration has increasingly recognized the presence of economically significant resources in non-volcanic settings, commonly referred to as non-volcanic geothermal systems [3–5]. These systems occur in areas lacking recent or active volcanism and are typically governed by alternative heat sources and fluid circulation mechanisms. The growing interest in non-volcanic geothermal is driven by several factors, including the need to expand geothermal development beyond volcanic provinces, the increasing demand for low-carbon heat and electricity, and improvements in geophysical and numerical methods that enable better characterization of deeper and more subtle geothermal targets [6, 7].

* Corresponding author.
E-mail address: salsabsiregar@gmail.co (S. Siregar).

https://doi.org/10.58524/jograv.v1i1.105
Received 4 January 2026; Received in revised form 6 February 2026; Accepted 15 February 2026
Available online 4 March 2026
XXXX-XXXX/Published by FoundAE (Foundation of Advanced Education).

Non-volcanic geothermal systems can be broadly categorized into several types based on their heat sources and geological context. These include (i) sedimentary basin geothermal systems, where heat is associated with normal geothermal gradients, deep fluid circulation, and basin-scale permeability pathways; (ii) crystalline basement systems, where elevated radiogenic heat production and fracture permeability may support geothermal circulation; and (iii) granite-related geothermal systems, where granitic intrusions contribute long-lived heat due to high concentrations of heat-producing elements such as uranium, thorium, and potassium [8–10]. In many regions, these categories overlap. For example, sedimentary basins may be underlain by granitic basement, and the geothermal regime may reflect both deep conductive heat flow and convective circulation along faults and fractures [3, 11]. Such complexity is often the defining characteristic of non-volcanic geothermal environments [12, 13].

A key challenge in non-volcanic geothermal exploration is the difficulty of identifying and constraining subsurface heat sources and reservoir geometries. In volcanic geothermal systems, heat sources are commonly inferred from volcanic history, geochemistry, and the presence of young intrusive bodies. In contrast, non-volcanic geothermal systems may be driven by older, buried intrusions or by regional-scale heat flow, which are not easily detectable at the surface [6, 14, 15]. Furthermore, reservoir permeability in non-volcanic settings is frequently controlled by fault systems, basement fractures, and lithological contrasts rather than by volcanic conduits or caldera structures [4, 16]. As a result, exploration uncertainty is often higher, leading to increased financial risk and slower development rates compared with volcanic geothermal provinces [17, 18]. This has important implications for geothermal development strategies in countries where large areas are non-volcanic but potentially geothermal.

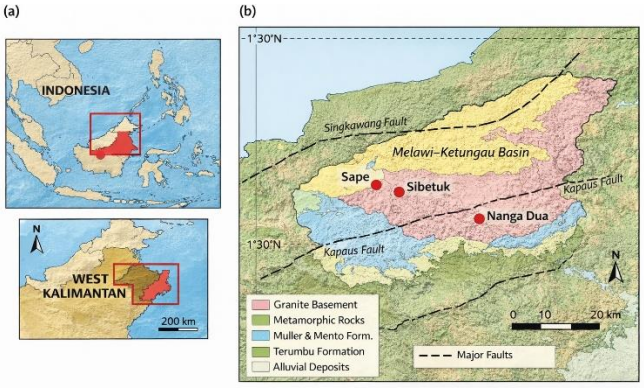

Fig. 1. (a). Location of West Kalimantan within Indonesia; (b). Geological map of the study area showing the Melawi-Ketungau basin, granite basement and geothermal prospect location: Sape, Sibetuk, and Nanga Dua.

2. Conceptual geological setting

2.1. *Non-volcanic geothermal systems and the role of granitic heat sources*

Granite-related geothermal systems have attracted growing attention because granitic rocks often exhibit elevated radiogenic heat production relative to other crustal lithologies [3, 6, 16]. The abundance of heat-producing elements can generate a sustained heat source over geological time scales, even in the absence of recent magmatic activity. In many cases, granitic bodies are emplaced at shallow to mid-crustal depths and may be partially concealed beneath sedimentary sequences. Where suitable permeability pathways exist—such as fault zones, fracture networks, or lithological boundaries—groundwater may circulate to depth, become heated, and return to the surface as thermal springs or warm wells [19–21]. This mechanism is consistent with non-volcanic geothermal manifestations observed in several continental regions worldwide.

In sedimentary basins, geothermal anomalies may also arise due to basin-scale hydrodynamics and pressure gradients. Deep groundwater circulation can be driven by topographic gradients, compaction-driven flow, or regional stress fields. When such flow intersects zones of enhanced permeability (e.g., fault corridors), it may produce localized thermal anomalies and geothermal discharge. Importantly, these mechanisms do not require anomalously high heat flow; instead, they rely on deep circulation that accesses warmer crustal temperatures at depth [3, 6, 16]. This is particularly relevant in non-volcanic regions where heat flow is moderate but geothermal manifestations are present. Therefore, distinguishing between granite-related heat sources and basin-driven circulation becomes critical for building accurate geothermal conceptual models.

From an exploration perspective, granite-related systems are especially challenging because the heat source is not necessarily expressed as a surface feature. Granitic intrusions may be deeply buried, and their geometry, depth, and extent can only be inferred through geophysical observations. Additionally, geothermal reservoirs in such systems may occur in sedimentary layers, fractured basement, or at the interface between sedimentary cover and crystalline basement [6, 14, 15]. This complexity demands integrated interpretation approaches combining geological mapping, geochemistry, and multiple geophysical methods.

2.2. Geological setting and geothermal prospects in West Kalimantan

West Kalimantan is characterized by a complex geological framework involving sedimentary basins, metamorphic units, and intrusive igneous bodies. The regional tectonic history includes multiple phases of deformation and magmatism, resulting in a heterogeneous crustal structure. The Melawi–Ketungau Basin represents a significant sedimentary domain, and its boundaries are likely controlled by major fault systems. These faults may act as conduits for deep fluid circulation, enabling geothermal manifestations at the surface [19–21].

The three geothermal prospects investigated in this study—Sape, Sibetuk, and Nanga Dua—are located within West Kalimantan and represent distinct geological environments (Fig. 1). Preliminary observations indicate differences in surface lithology and geothermal manifestation characteristics among these prospects. However, surface geology alone is insufficient to determine the subsurface heat sources and reservoir configurations. For instance, the presence of granite at or near the surface may indicate a heat source, but the geothermal system may still be controlled by deeper intrusions or by basin-scale circulation. Conversely, geothermal manifestations occurring in sedimentary areas may be influenced by buried granitic bodies that are not exposed at the surface. Therefore, constraining the subsurface lithological distribution and structural framework is essential.

3. Method

3.1. *Study area and data source*

This study was conducted from October 2022 to May 2023 in West Kalimantan Province, Indonesia, focusing on three non-volcanic geothermal manifestation areas: Sape, Sibetuk, and Nanga Dua. All data processing and interpretation were carried out at the Geophysics Laboratory, Physics Study Program, Department of Science, Institut Teknologi Sumatera. The study area is located within the coordinate range of 0°01′18.40″N–1°48′57.86″N and 110°28′20.64″E–113°05′39.11″E (Fig. 2). Secondary datasets were utilized in this research.

Satellite-derived gravity and topographic data, including latitude, longitude, elevation, and free-air anomaly (FAA), were obtained from the TOPEX website (https://topex.ucsd.edu) on 14 December 2022. A 30 m-resolution DEM SRTM dataset for Indonesia (released in 2014) was acquired from https://indonesia-geospasial.com and used to generate inner-grid and outer-grid parameters required for terrain correction. Geological information was obtained from the Geological Map of the Sintang and Sanggau sheets (1993), accessed through the ESDM GeoMap portal (https://geologi.esdm.go.id/geomap), providing supporting data on lithology, stratigraphy, and the age of rock formations within the study area.

The workflow began with a literature review of non-volcanic geothermal systems and the regional geological framework of West Kalimantan, followed by delineation of the study boundary using Google Earth Pro. The coordinate range was converted into decimal format using the standard conversion formula and subsequently applied to extract FAA and elevation data from TOPEX. Initial processing was performed in Microsoft Excel to compile the datasets and calculate the simple Bouguer anomaly (SBA).

Terrain correction parameters were then generated using Global Mapper based on the 30 m DEM by separating inner-grid and outer-grid areas. The main gravity processing was conducted in Oasis Montaj, where the dataset was converted into UTM Zone 49N prior to applying terrain correction. The terrain correction results were combined with SBA to produce the complete Bouguer anomaly (CBA).

Regional and residual anomalies were separated using Butterworth and bandpass filters, and the filtered results were used for two-dimensional (2D) forward modeling. For three-dimensional (3D) modeling, the CBA dataset was gridded using Surfer to obtain a continuous anomaly surface and subsequently modeled in Grablox. Density parameters were adjusted based on reference rock densities and regional geological constraints to obtain the most plausible subsurface configuration. Interpretation was carried out using both qualitative and quantitative approaches by integrating gravity anomaly patterns with the 2D–3D modeling results and comparing them with the regional geological map, particularly in terms of lithological distribution and major structural features that may control geothermal fluid circulation.

3.2. *Gravity data processing*

Gravity data processing was conducted in two main stages: (1) gravity correction and Complete Bouguer Anomaly (CBA) calculation, and (2) anomaly separation and subsurface modeling. [14, 22, 23]. The raw dataset consisted of Free Air Anomaly (FAA) values. To obtain the Complete Bouguer Anomaly (CBA), the following corrections were applied:

- Free Air Correction (FAC)
- Bouguer Slab Correction
- Terrain Correction (TC)

The Bouguer correction accounts for the gravitational effect of the rock mass between the observation point and the reference datum. Terrain correction compensates for topographic variations surrounding measurement points and was computed using SRTM elevation data.

An optimal Bouguer density was estimated through correlation analysis between elevation and Bouguer anomaly values using density variations ranging from 1.7 to 2.3 g/cm³. The density value that minimized correlation between gravity anomaly and elevation was selected as the representative surface density. The Complete Bouguer Anomaly (CBA) was calculated as:

$$CBA = FAA - Bouguer\ Correction + Terrain\ Correction \quad \ldots (1)$$

The corrected dataset was subsequently converted into UTM Zone 48S coordinates for spatial analysis.

3.3. *Spectral analysis and regional–residual separation*

To estimate source depth and separate regional and residual components, spectral analysis was performed using fourier transform techniques implemented in Oasis Montaj. The logarithmic power spectrum was analyzed by plotting log amplitude against wavenumber. The slope of the spectrum was used to estimate the average depth of anomaly sources. A cut-off wavenumber was determined based on the transition between deep (regional) and shallow (residual) sources, supported by the coefficient of determination (R^2) as a control parameter. Regional and residual anomalies were separated using frequency-domain filtering:

- Low-pass filter → isolates deep regional anomalies
- Band-pass filter → highlights shallow residual anomalies

Residual anomalies are interpreted to represent shallow density contrasts related to structural features and geothermal circulation pathways.

3.4. *Two and three-dimensional forward modeling*

Two-dimensional forward modeling was conducted along selected profiles crossing significant gravity anomalies. The objective was to estimate subsurface geometry and density distribution consistent with observed gravity responses. Modeling was performed using Oasis Montaj, integrating geological constraints. A trial-and-error forward modeling approach was applied until the misfit between observed and calculated anomalies was minimized (error <5%). The minimum and maximum density values obtained from 2D modeling were used as constraints for subsequent 3D inversion modeling.

Three-dimensional gravity modeling was performed using Grablox 1.6e, with visualization in Bloxer 1.6e. The workflow consisted of:

1. Initial Forward Modeling
   A block model representing the study area was constructed based on gridded Complete Bouguer Anomaly data. Major and minor blocks were defined according to spatial resolution and area extent.
2. Density Parameter Assignment
   Density values derived from 2D modeling were assigned as initial constraints.
3. Inverse Modeling
   An iterative inversion procedure was applied to adjust density distribution and geometry to minimize misfit between observed and calculated gravity anomalies. Optimization stages included:
   - Base model adjustment
   - Density optimization
   - Occam density smoothing
   - Elevation adjustment
   - Occam height smoothing

The inversion process aimed to reduce residual error and obtain a geologically reasonable subsurface density model.

3.5. *Data interpretation*

Interpretation was conducted qualitatively and quantitatively. For the qualitative interpretation, gravity anomaly maps (Complete Bouguer, regional, and residual) were analyzed to identify patterns associated with density contrasts. High gravity anomalies were interpreted as potential granitoid intrusions or basement highs, whereas low residual anomalies were interpreted as fractured or altered zones possibly associated with geothermal fluid pathways.

While quantitative interpretation, the cross-sectional models from 2D forward modeling and volumetric density distributions from 3D inversion were integrated with geological maps. Density contrasts were correlated with lithological units and structural features, particularly fault systems that may act as geothermal conduits.

- The final interpretation focuses on identifying:
- Potential granite heat sources
- Structural controls (faults/fractures)
- Zones of reduced density indicative of hydrothermal alteration

4. Results and discussion

The gravity data used in this study were secondary datasets obtained from the TOPEX website (https://topex.ucsd.edu). The dataset includes longitude, latitude, elevation, and free-air anomaly (FAA) values at each observation point within the study area. The extracted data were first compiled and processed in Microsoft Excel to perform the Bouguer correction. From this calculation, an average reduction density of 0.931 g/cm³ was obtained and subsequently applied to compute the Simple Bouguer Anomaly (SBA).

In the initial Bouguer correction stage, the study area is assumed to be a flat horizontal surface. However, in reality, the terrain is characterized by significant undulations, including valleys and hills, which affect the measured gravitational acceleration. Therefore, terrain correction was required to eliminate the influence of surrounding topographic variations. The topographic map of the study area (Fig. 2) shows that the northeastern and southeastern parts are characterized by relatively high elevations ranging from approximately 300 m to 850 m above sea level. In contrast, geothermal manifestations are generally located in relatively flat areas with elevations between 50 m and 150 m.

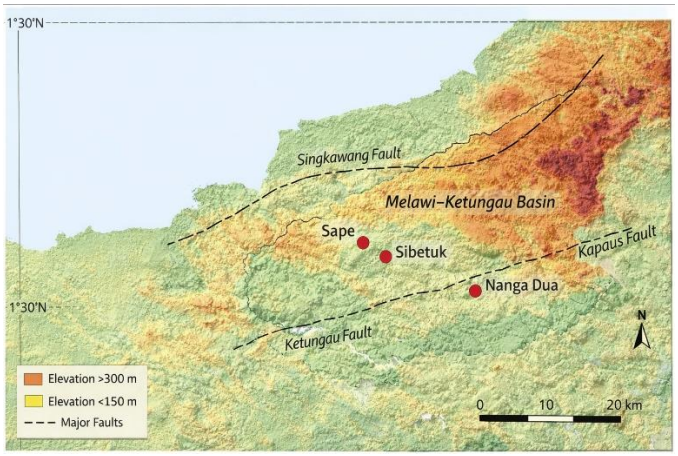

Fig. 2. Topographic map of the study area in West Kalimantan, Indonesia, showing elevation variations and the locations of the Sape, Sibetuk, and Nanga Dua geothermal prospects. Areas with elevations greater than 300 m are concentrated in the northeastern and southeastern parts of the region, while geothermal manifestations are generally located in relatively low-elevation areas (50–150 m above sea level).

Terrain correction was performed using Oasis Montaj software. Elevation data were obtained from the Indonesia Geospatial portal (https://indonesia-geospasial.com) in the form of 30 m resolution DEM SRTM data covering the entire Indonesian region. The DEM, together with the longitude and latitude data, was processed in Global Mapper to determine the inner-grid and outer-grid parameters required for terrain correction. These parameters were subsequently imported into Oasis Montaj to calculate the terrain correction values. Finally, the terrain correction values were added to the Simple Bouguer Anomaly to obtain the Complete Bouguer Anomaly (CBA), which was used for further analysis and modeling [24].

4.1. Complete bouguer anomaly (CBA)

The Complete Bouguer Anomaly (CBA) represents the subsurface mass distribution obtained after applying all necessary gravity corrections, including free-air, Bouguer slab, and terrain corrections. The CBA map was generated through data gridding using Oasis Montaj. As shown in Fig. 3, the anomaly values range from 12 mGal to 51.7 mGal, indicating significant lateral density variations across the study area).

High anomaly values are predominantly distributed in the northeastern and southeastern parts of the region, which also correspond to areas of relatively high elevation. These high-anomaly zones are interpreted as being associated with high-density igneous or crystalline basement rocks. In contrast, lower anomaly values are observed in areas surrounding the geothermal prospects and are interpreted as sedimentary rocks with relatively lower densities.

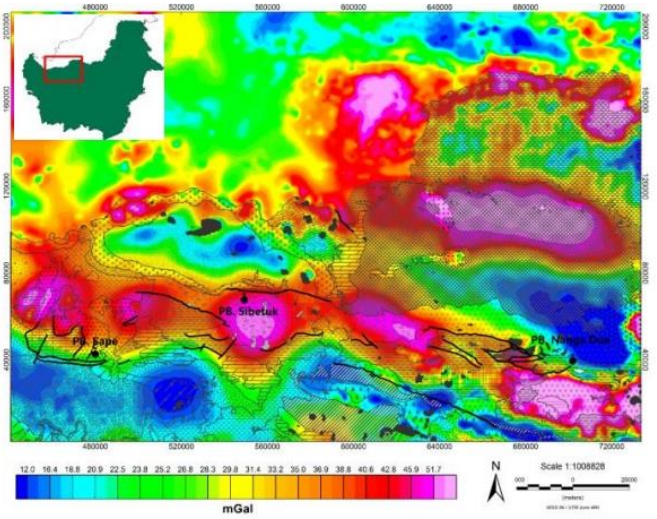

Fig. 3. Overlay the ABL map with the geological map of the study area.

Low gravity anomalies are distributed across the northern, southern, and eastern parts of the study area. These low-anomaly zones predominantly occupy the Melawi Basin and Ketungau Basin, as shown in Fig. 4. In contrast, high anomaly zones are mainly concentrated in the northwestern and northeastern sectors and extend as a belt cutting across the low-anomaly region from the west toward the southeast. The overlay between the gravity anomaly map and the sedimentary basin boundaries indicates that the Sape and Nanga Dua geothermal prospects are located within the sedimentary basin domain, whereas the Sibetuk prospect is situated outside the basin.

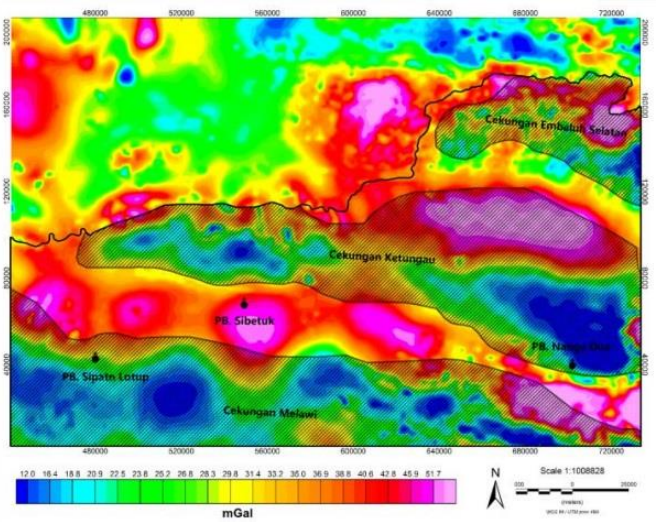

Fig. 4. Overlay the ABL map with the sediment basin map.

The low anomaly zone ranges from 12 mGal to 22.5 mGal and is represented by dark blue to light green colors on the map. Moderate anomaly values range from 22.5 mGal to 31.4 mGal, indicated by light green to yellow colors. High anomaly values range from 31.4 mGal to 51.7 mGal and are represented by orange

to purple colors. The CBA map further shows that the geothermal manifestations are located within or adjacent to high-anomaly zones. Therefore, these high-density anomaly areas are interpreted as potential heat sources, likely related to granitic or crystalline basement bodies that control the geothermal system in the study area.

As illustrated in Fig. 5, the basin areas where the Sape and Nanga Dua geothermal manifestations occur are dominated by Tertiary formations composed mainly of sedimentary rocks. Conversely, the Sibetuk geothermal prospect is located within a high-anomaly zone associated with the Semitau Complex, which is dominated by granitic lithologies. The presence of Carboniferous granitic rocks in the Semitau Complex provides a geological basis for interpreting the high Bouguer anomaly values in the study area as being related to granite bodies [20, 21, 25].

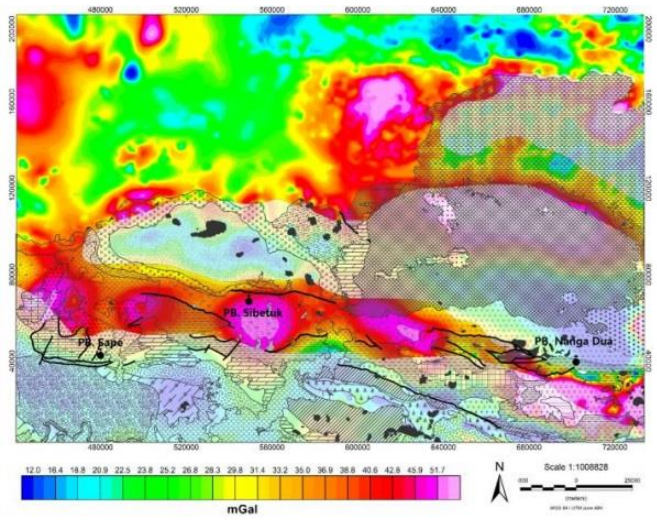

Fig. 5. Overlay the ABL map with the geological map and sedimentary basin map.

Based on geological constraints, the Semitau Complex exhibits very high Bouguer anomaly values, ranging from approximately 45.9 mGal to 51.7 mGal. These anomalies are interpreted to reflect the response of high-density crystalline rocks, particularly granitic units. However, the complete Bouguer anomaly map still represents a combined response of both regional and residual components. As a result, geological lineaments and basin-scale structural patterns are not clearly resolved. Residual anomalies generally represent shallow sources, whereas regional anomalies are related to deeper and broader subsurface structures. Separating these components is therefore necessary to reduce ambiguity and improve the reliability of subsequent 2D and 3D forward modeling [16, 26, 27].

4.2. *Spectral analysis*

Spectral analysis was applied to estimate the depths of regional and residual sources derived from the Complete Bouguer Anomaly (CBA) data. This method is performed in the frequency domain. Therefore, the gravity anomaly data, which are initially represented in the spatial domain, were transformed into the frequency domain using the Fourier transform. The resulting wavenumber (k) and amplitude (A) spectra were then analyzed to determine the depth of causative sources.

In the logarithmic power spectrum, different linear segments correspond to anomaly sources at varying depths. The slope of each segment is used to estimate the average depth of the corresponding geological source. This analysis also provides a basis for determining the appropriate filter window width for separating regional and residual anomaly components, as illustrated in Fig. 6. The estimated depths derived from the spectral method were subsequently used to constrain the filtering parameters and improve the reliability of anomaly separation prior to forward modeling.

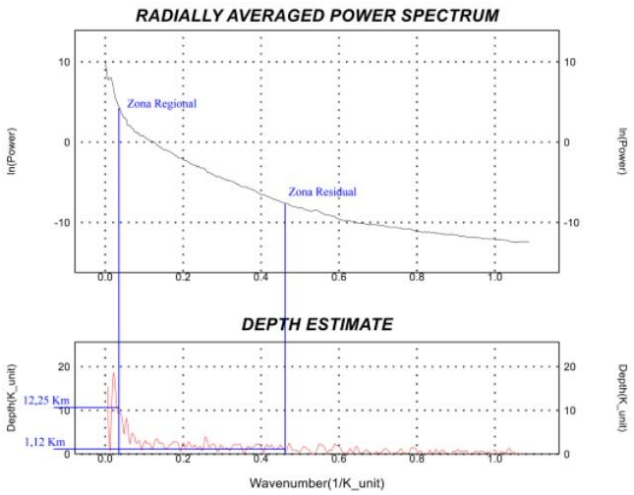

Fig. 6. Radially average spectrum curve and depth estimation.

To obtain the contour maps of regional and residual anomalies, the Complete Bouguer Anomaly (CBA) dataset was first subjected to filtering. This process was performed not only to separate the regional and residual components but also to reduce high-frequency noise within the shallow anomaly signal. A Butterworth filter was applied to isolate the regional and residual anomaly components based on their respective frequency characteristics. The regional anomaly represents low-frequency signals with long wavelengths, which are generally associated with deeper and broader subsurface structures.

As shown in Fig. 7, the regional anomaly map reveals a pattern of low anomalies occupying the sedimentary basin areas. These low-anomaly zones correspond to rock formations dominated by sedimentary lithologies such as siltstone, mudstone, and sandstone. The relatively low average density of these sedimentary rocks results in negative or lower gravity responses within the basin domain.

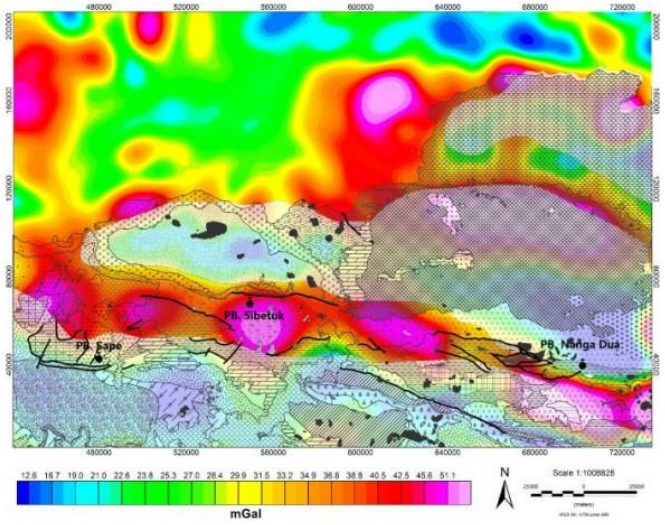

Fig. 7. Overlay regional anomaly maps with geological and sedimentary basin maps.

The residual anomaly map was obtained by subtracting the regional anomaly component from the Complete Bouguer Anomaly. Prior to interpretations, a bandpass filter was applied to further suppress noise and enhance the high-frequency signals. The residual anomaly primarily reflects shallow geological sources characterized by shorter wavelengths and higher frequencies. These higher-frequency anomalies are associated with lateral lithological variations and near-surface structural heterogeneities. Therefore, the residual anomaly map is particularly useful for identifying local geological structures and delineating features that may control geothermal fluid circulation in the study area.

4.3. 2D gravity anomaly modeling

Two-dimensional (2D) modeling was performed by extracting profile slices from the Complete Bouguer Anomaly (CBA) map. The lithological interpretation of each modeled unit was constrained using the regional geological map and reference rock density values (Table 1). Three profiles were selected for modeling, each intersecting at least two geothermal prospects. These profiles are designated as A–A', B–B', and C–C', as shown in Fig. 8. Profile A–A' extends from southwest to northeast with a total length of approximately 312 km, crossing the Sape and Sibetuk geothermal prospects and the Melawi–Ketungau Basin. Profile B–B' trends west to east with a length of 251 km and intersects the Sape and Nanga Dua prospects. Profile C–C' extends from northwest to southeast over a distance of 264 km, crossing the Sibetuk and Nanga Dua prospects.

Table 1
Rock density values

Rock Type	Lithology	Density Range (g/cm³)	Average Density (g/cm³)
Sedimentary rocks	Alluvium	1.96 – 2.00	1.98
	Limestone	1.20 – 2.40	1.29
	Soil	1.53 – 2.60	2.00
	Clay	1.63 – 2.67	2.21
	Gravel	1.70 – 2.40	2.00
	Sand	1.70 – 2.30	2.00
	Sandstone	1.61 – 2.76	2.35
	Shale	1.77 – 3.20	2.40
	Limestone	1.93 – 2.90	2.55
	Dolomite	2.28 – 2.90	2.70
Igneous rocks	Rhyolite	2.35 – 2.70	2.52
	Andesite	2.40 – 2.80	2.61
	Granite	2.50 – 2.81	2.64
	Diorite	2.72 – 2.99	2.85
	Lava	2.80 – 3.00	2.90
	Basalt	2.70 – 3.30	2.99
	Gabbro	2.70 – 3.50	3.03
Metamorphic rocks	Graywacke	2.26 – 2.70	2.65
	Slate	2.70 – 2.90	2.79
	Gneiss	2.59 – 3.00	2.80
	Amphibolite	3.20 – 3.54	3.37
	Metamorphic	2.40 – 3.10	2.74

The 2D modeling was conducted using a forward modeling approach implemented in the GM-SYS module of Oasis Montaj. In this method, subsurface layer geometries were iteratively adjusted until the calculated gravity response matched the observed anomaly data. The modeling process was constrained by three main elements: the observed anomaly curve (black dots), the calculated anomaly curve (black line), and the error curve (red line). Density values assigned to each geological unit directly influence the calculated gravity response, such that higher average densities produce higher gravity anomalies.

Fig. 9 presents the 2D model along profile A–A', which consists of 13 geological units and yields a modeling error of 2.616%. The Semitau Complex, formed during the Carboniferous period, acts as the basement unit and is interpreted as the sub-basement of the Ketungau Basin. This complex consists of green schist, granite, granodiorite, and diorite, and was modeled with an average density of 2.61 g/cm³, indicating dominance of granitic lithologies. The Balaisebut Complex, also of Carboniferous age, was modeled as a metamorphic unit composed of slate, mudstone, shale, fine sandstone, quartzite phyllite, limestone, and schist, with an average density of 2.61 g/cm³, suggesting a predominance of slate. Both complexes are overlain by the Selangkai group (late cretaceous), composed of shale, mudstone, sandstone, conglomerate, and limestone. This unit exhibits an average modeled density of 2.68 g/cm³ and is interpreted to be sandstone-dominated.

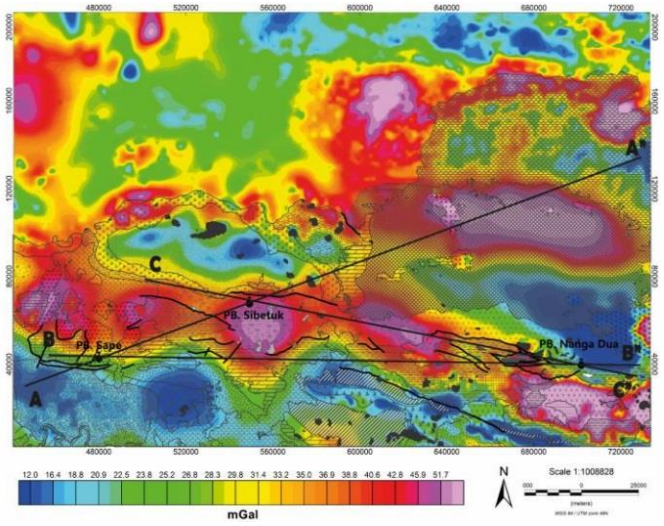

Fig. 8. Line A-A, B-B, and C-C on the complete bouguer anomaly map.

During the Tertiary period (late eocene–early oligocene), significant sedimentation occurred, leading to the formation of the Ketungau and Melawi Basins. The Ketungau Basin comprises the Kantu Formation, Tutoop Sandstone, and Ketungau Formation, consisting of mudstone, siltstone, sandstone, and thin coal layers. The modeled average densities are 2.55 g/cm³ for the Kantu Formation, 2.41 g/cm³ for Tutoop Sandstone, and 2.68 g/cm³ for the Ketungau Formation. The Melawi Basin includes the Payak, Tebidah, and Sekayam Sandstone formations, which are composed mainly of sandstone, siltstone, mudstone, and locally thin coal layers. Quaternary deposits unconformably overlie the older formations. These consist of alluvium and incised alluvium, with average densities of 2.09 g/cm³ and 1.94 g/cm³, respectively. These unconsolidated deposits are composed of mud, sand, gravel, and organic material and were modeled as the uppermost layers in the subsurface configuration.

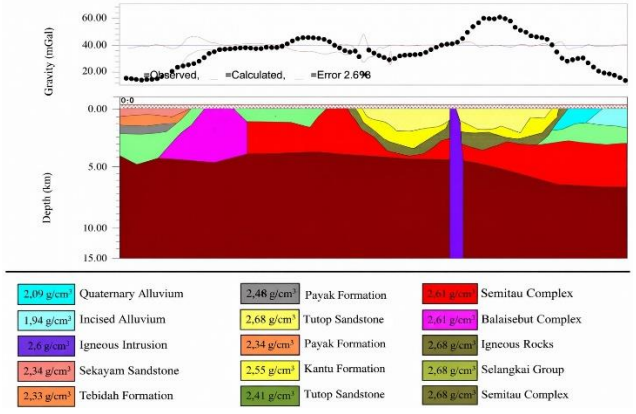

Fig. 9. Results of layer modelling on line A-A'.

Subsequent 2D modeling was performed along profiles B–B' and C–C', as shown in Fig. 10, to evaluate lateral variations in subsurface structure and lithological distribution across the geothermal prospects. The 2D forward model along profile B–B', which consists of 10 geological units and yields a modeling error of 2.335%. This profile intersects the Sape and Nanga Dua geothermal prospects and shows several formations that are also present along profile A–A', including the Balaisebut Complex, Semitau Complex, Selangkai Group, and Ketungau Formation. In addition, profile B–B' includes the Embuoi Complex, which formed during the Permian to Triassic period. This complex comprises granite, granodiorite, schist, basic volcanic rocks, and amphibolite. The modeled average density for this unit is 2.59 g/cm³, indicating that the Embuoi Complex is predominantly composed of granitic lithologies.

The Busang Complex, formed during the Permian, is also identified along this profile. It consists mainly of granite, granodiorite, and gabbro and was modeled with a dark blue color. The forward modeling results indicate an average density of 2.68 g/cm³, suggesting a dominance of granitic to intermediate intrusive rocks. The Piyabun Volcanic Group, formed during the Middle Eocene, is composed primarily of tuff and agglomerate. This unit was modeled in yellow and exhibits an average density of 2.61 g/cm³ based on the modeling results.

The Mandai Group, deposited during the Early Oligocene, consists of sandstone, mudstone, and siltstone. In the model, this formation is represented by a brown layer and has an average density of 2.31 g/cm³, indicating a predominance of sandstone. The Silat Shale Formation, also of Early Oligocene age, comprises mudstone, carbonaceous shale, siltstone, and sandstone. This unit is represented by a dark gray layer in the model and exhibits an average density of 2.44 g/cm³. The modeled density suggests that this formation is dominated by mudstone [28, 29].

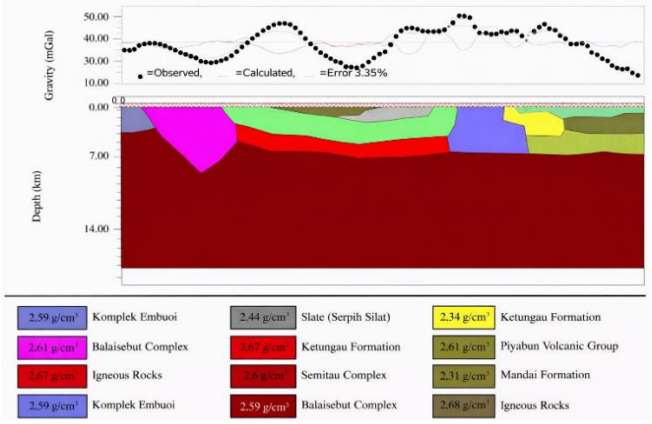

Fig. 10. Results of layer modelling on line B-B'.

Fig. 11 shows the 2D forward model along profile C–C', which consists of eight geological units and yields a modeling error of 2.693%. The subsurface configuration along this profile is generally similar to that obtained for profile B–B'. In the C–C' model, an igneous unit is consistently interpreted as the lowermost layer. This igneous basement is represented by a dark red layer and was assigned an average density of 2.70 g/cm³. The relatively high density suggests that this unit is dominated by crystalline igneous rocks, most likely granite and/or ophiolitic components [16].

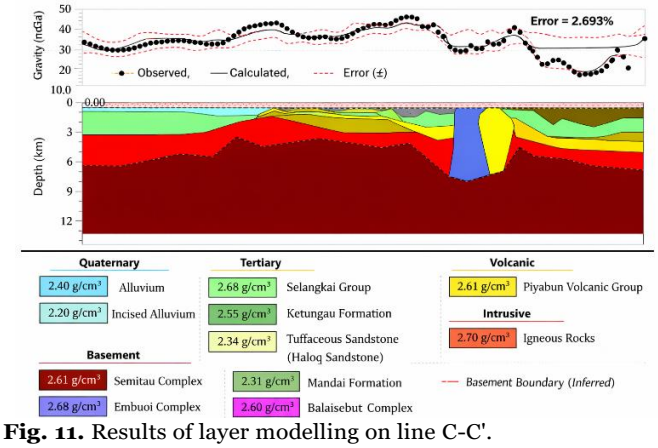

Fig. 11. Results of layer modelling on line C-C'.

4.4. 3D modelling of gravity anomalies

In the 3D modeling of ABL map data (longitude, latitude, and ABL values), the dataset was first subjected to a gridding process using Surfer software. This step aimed to regularize the irregular spatial distribution of data points caused by varying distances between randomly distributed measurement locations. The gridded data were then used to generate surface contour maps.

The 3D modeling process was continued through inversion using Grablox software, where the gridded data served as input. Several optimization stages were applied during the inversion process, including base optimization, density optimization, height optimization, Occam density (d), and Occam height (h). These optimization steps were performed to minimize the modeling error and improve the accuracy of the resulting model.

Before optimization, the density range determined from the 2D modeling was defined as a constraint for the inversion process. In this study, the density range was set between 1 and 3 g/cm³. Base optimization was carried out to refine the fundamental anomaly parameters. Density optimization aimed to adjust the calculated density values to better match the observed data. Height optimization and Occam height regularization were applied to stabilize and maximize the vertical distribution of each block within the model.

A lower error value indicates a better agreement between observed and calculated data, suggesting higher model reliability. After completing all inversion and optimization steps, the final 3D model was visualized using Bloxer software.

Based on the 3D modeling results shown in Fig. 12, the study area exhibits rock density values ranging from 1 to 3 g/cm³. The modeled layers (layers 1–10) extend to a depth of approximately 18.37 km along the Z-direction. Density variations are represented using a color scale in the 3D model visualization. The upper surface of the 3D model is predominantly characterized by sedimentary rocks, with density values ranging from approximately 1.57 to 2.5 g/cm³.

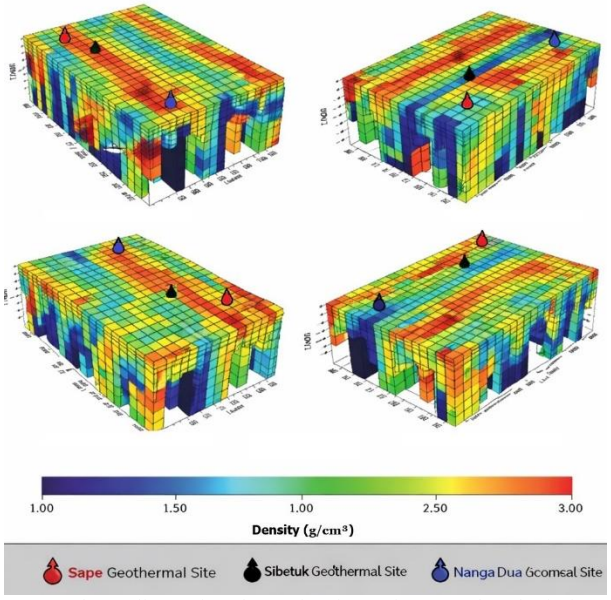

Fig. 12. Three-dimensional gravity inversion results depicting the subsurface density distribution of the Sape, Sibetuk, and Nanga Dua geothermal systems.

The sixth layer model is located at a depth of approximately 4–6 km, with density values ranging from 1 to 3 g/cm³ (Fig. 13). Within this layer, basin structures are clearly identified by the presence of very low-density zones, ranging from 1 to 1.55 g/cm³. These low-density anomalies likely represent sedimentary accumulations filling structural depressions. In addition, a prominent high-density zone is observed separating two elongated basin structures. This high-density anomaly is interpreted to correspond to lithological units dominated by dense igneous rocks such as granite, granodiorite, diorite, and ophiolitic complexes. The high-density values range from approximately 2.8 to 3 g/cm³, indicating the presence of compact and crystalline basement or intrusive bodies.

Based on the 2D modeling results, the regional depth was estimated at approximately 12.25 km. At this regional depth, the anomaly pattern appears relatively homogeneous compared to shallower layers. Fig. 14 presents the ninth layer model, corresponding to depths of approximately 11–13 km.

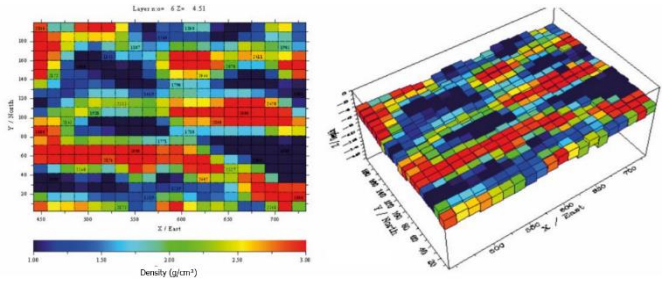

Fig. 13. 3D modelling of the sixth layer.

The ninth layer exhibits a more uniform density distribution overall. However, the density values can still be categorized into two dominant groups: very high-density zones and very low-density zones. The high-density regions, ranging from 2.8 to 3 g/cm³, are interpreted as intrusive or crystalline igneous rocks forming part of the basement structure. In contrast, the low-density zones, ranging from 1 to 1.7 g/cm³, are interpreted as sedimentary formations. These results suggest a clear vertical differentiation between shallow sedimentary basin structures and deeper high-density igneous basement units, reflecting the regional tectonic and magmatic framework of the study area [16].

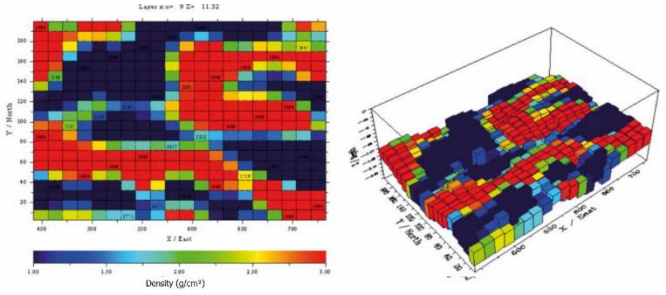

Fig. 14. 3D modelling of the ninth layer.

5. Conclusion

Based on the results of this study, the subsurface structures of the Sape, Sibetuk, and Nanga Dua geothermal areas have been successfully modeled using 3D inversion techniques. The interpreted heat source is estimated to occur at a depth of approximately 6 km and is likely associated with granitic intrusive rocks. The Sape geothermal system is inferred to be hosted predominantly within slate formations with an average density of about 2.6 g/cm³. In contrast, the Sibetuk geothermal system is interpreted to overlie granitic formations with a similar density of approximately 2.6 g/cm³, while the Nanga Dua geothermal system is associated mainly with sandstone formations with an average density of 2.31 g/cm³. The significant contrast in density distribution across the study area suggests strong structural heterogeneity, which likely contributed to the development of numerous fault structures controlling fluid migration. Furthermore, the 3D modeling results indicate the presence of low-density anomalies ranging from 1 to 2 g/cm³, which are interpreted as Tertiary sedimentary basins. Meanwhile, high-density anomalies ranging from 2.6 to 3 g/cm³ are interpreted as uplifted igneous rocks forming part of the regional basement. These findings highlight the structural and lithological controls influencing the geothermal systems in the study area.

CRediT authorship contribution statement

Salsabila Siregara: Writing – review & editing, Writing – original draft, Supervision, Software, Resources, Methodology, Investigation, Formal analysis, Data curation. **Berwyn Dzaky Radhitya:** Writing – review & editing, Supervision, Resources, Methodology, Investigation, Formal analysis, Data curation, Conceptualization.

Declaration of Competing Interest

The authors declare that they have no known competing financial interests or personal relationships that could have appeared to influence the work reported in this paper.

Data availability

Data will be made available on request.

Acknowledgment

The authors would like to express their sincere gratitude to all parties who supported this research. The authors also acknowledge the institutions and local authorities involved in facilitating field data acquisition in the Sape, Sibetuk, and Nanga Dua geothermal areas. Their cooperation and assistance were essential to the successful completion of this research. We are grateful to colleagues and research collaborators for their valuable discussions and constructive suggestions during the modeling and interpretation stages. Finally, the authors appreciate the reviewers and editors for their insightful comments and recommendations, which significantly improved the quality of this manuscript.

References

1. Hosono, T., Hartmann, J., Louvat, P., Amann, T., Washington, K. E., West, A. J., Okamura, K., Böttcher, M. E., and Gaillardet, J. (2018). Earthquake-Induced Structural Deformations Enhance Long-Term Solute Fluxes from Active Volcanic Systems, *Scientific Reports*, Vol. 8, No. 1, 1–12. doi:10.1038/s41598-018-32735-1.
2. Zhang, Z., Yao, H., Wang, W., and Liu, C. (2021). 3-D Crustal Azimuthal Anisotropy Reveals Multi-Stage Deformation Processes of the Sichuan Basin and Its Adjacent Journal of Geophysical Research : Solid Earth, *Journal of Geophysical Research: Solid Earth*, Vol. 127, No. e2021JB023289, 1–17. doi:10.1029/2021JB023289.
3. Liu, S., Suardi, I., Xu, X., Yang, S., and Tong, P. (2021). The Geometry of the Subducted Slab Beneath Sumatra Revealed by Regional and Teleseismic Traveltime Tomography, *Journal of Geophysical Research: Solid Earth*, Vol. 126, No. 1, 1–29. doi:10.1029/2020JB020169.
4. Dewi, K. C. S., Siregar, R. N., Ningati, T. I., Pulungan, Z. N., Indriyawati, A., and Takahashi, H. (2025). Analysis of Subsurface Faults Using 3D Gravity Method Based On Satellite Image Data : Insights into Indo-Australian and Eurasian Plate Subduction in the Formation of An Accretionary Prism, *International Journal of Hydrological and Environmental for Sustainability*, Vol. 4, No. 3, 135–148.
5. Hariyono, E., and S, L. (2018). The Characteristics of Volcanic Eruption in Indonesia, *Volcanoes - Geological and Geophysical Setting, Theoretical Aspects and Numerical Modeling, Applications to Industry and Their Impact on the Human Health*, No. July. doi:10.5772/intechopen.71449.
6. McCaffrey, R. (2009). The Tectonic Framework of the Sumatran Subduction Zone, *Annual Review of Earth and Planetary Sciences*, Vol. 37, 345–366. doi:10.1146/annurev.earth.031208.100212.
7. Hristov, V., Stoyanov, N., Valtchev, S., Kolev, S., and Benderev, A. (2019). Utilization of Low Enthalpy Geothermal Energy in Bulgaria, *IOP Conference Series: Earth and Environmental Science*, Vol. 249, No. 1. doi:10.1088/1755-1315/249/1/012035.
8. Taruna, R. M., and Banyunegoro, V. H. (2018). Earthquake Relocation Using Double Difference Method for 2D Modelling of Subducting Slab and Back Arc Thrust in West Nusa Tenggara, *Jurnal Penelitian Fisika Dan Aplikasinya (JPFA)*, Vol. 8, No. 2, 132. doi:10.26740/jpfa.v8n2.p132-143.
9. Collings, R., Lange, D., Rietbrock, A., Tilmann, F., Natawidjaja, D., Suwargadi, B., Miller, M., and Saul, J. (2012). Structure and Seismogenic Properties of the Mentawai Segment of the Sumatra Subduction Zone Revealed by Local Earthquake Traveltime Tomography, *Journal of Geophysical Research*, Vol. 117, 1–23. doi:10.1029/2011JB008469.
10. Jihad, A., Muksin, U., Syamsidik, and Ramli, M. (2021). Earthquake Relocation to Understand the Megathrust Segments along the Sumatran Subduction Zone, *IOP Conference Series: Earth and Environmental Science*, Vol. 630, 012002. doi:10.1088/1755-1315/630/1/012002.
11. Xu, J., and Kono, Y. (2002). Geometry of Slab, Intraslab Stress Field and Its Tectonic Implication in the Nankai Trough, Japan, *Earth, Planets and Space*, Vol. 54, No. 7, 733–742. doi:10.1186/BF03351726.

12. Kusuhara, F., Kazahaya, K., Morikawa, N., Yasuhara, M., Tanaka, H., Takahashi, M., and Tosaki, Y. (2020). Original Composition and Formation Process of Slab-Derived Deep Brine from Kashio Mineral Spring in Central Japan, *Earth, Planets and Space*, Vol. 72, No. 1. doi:10.1186/s40623-020-01225-y.

13. Malod, J. A., Karta, K., Beslier, M. O., and Zen, M. T. (1995). From Normal to Oblique Subduction: Tectonic Relationships between Java and Sumatra, *Journal of Southeast Asian Earth Sciences*, Vol. 12, Nos. 1–2, 85–93. doi:10.1016/0743-9547(95)00023-2.

14. Li, C. F. (2011). An Integrated Geodynamic Model of the Nankai Subduction Zone and Neighboring Regions from Geophysical Inversion and Modeling, *Journal of Geodynamics*, Vol. 51, No. 1, 64–80. doi:10.1016/j.jog.2010.08.003.

15. Stern, R. J. (2002). Subduction Zones, *Reviews of Geophysics*, Vol. 40, No. 4, 3-1-3–38. doi:10.1029/2001RG000108.

16. Utama, H. W., Mulyasari, R., and Said, Y. M. (2021). Geothermal Potential on Sumatra Fault System To Sustainable Geotourism in West Sumatra, *JGE (Jurnal Geofisika Eksplorasi)*, Vol. 7, No. 2, 126–137. doi:10.23960/jge.v7i2.128.

17. Tabei, T., Hashimoto, M., Miyazaki, S., Hirahara, K., Kimata, F., Matsushima, T., Tanaka, T., Eguchi, Y., Takaya, T., Hoso, Y., Ohya, F., and Kato, T. (2002). Subsurface Structure and Faulting of the Median Tectonic Line, Southwest Japan Inferred from GPS Velocity Field, *Earth, Planets and Space*, Vol. 54, No. 11, 1065–1070. doi:10.1186/BF03353303.

18. Tongkul, F. (2017). Active Tectonics in Sabah – Seismicity and Active Faults, *Bulletin of the Geological Society of Malaysia*, Vol. 64, No. December, 27–36. doi:10.7186/bgsm64201703.

19. Maryanto, S. (2017). Geo Techno Park Potential at Arjuno-Welirang Volcano Hosted Geothermal Area, Batu, East Java, Indonesia (Multi Geophysical Approach), *AIP Conference Proceedings*, Vol. 1908, No. 2017. doi:10.1063/1.5012712.

20. Sujitapan, C., Kendall, J. M., Chambers, J. E., and Yordkayhun, S. (2024). Landslide Assessment through Integrated Geoelectrical and Seismic Methods: A Case Study in Thungsong Site, Southern Thailand, *Heliyon*, Vol. 10, No. 2. doi:10.1016/j.heliyon.2024.e24660.

21. Chambers, J., Holmes, J., Whiteley, J., Boyd, J., Meldrum, P., Wilkinson, P., Kuras, O., Swift, R., Harrison, H., Glendinning, S., Stirling, R., Huntley, D., Slater, N., and Donohue, S. (2022). Long-Term Geoelectrical Monitoring of Landslides in Natural and Engineered Slopes, *Leading Edge*, Vol. 41, No. 11, 768–767. doi:10.1190/tle41110768.1.

22. Whiteley, J. S., Watlet, A., Uhlemann, S., Wilkinson, P., Boyd, J. P., Jordan, C., Kendall, J. M., and Chambers, J. E. (2021). Rapid Characterisation of Landslide Heterogeneity Using Unsupervised Classification of Electrical Resistivity and Seismic Refraction Surveys, *Engineering Geology*, Vol. 290, No. May, 106189. doi:10.1016/j.enggeo.2021.106189.

23. Martinho, E. (2023). *Electrical Resistivity and Induced Polarization Methods for Environmental Investigations: An Overview*, *Water, Air, and Soil Pollution* (Vol. 234), Springer International Publishing. doi:10.1007/s11270-023-06214-x.

24. Kusumayudha, S. B., Lestari, P., and Paripurno, E. T. (2018). Eruption Characteristic of the Sleeping Volcano, Sinabung, North Sumatera, Indonesia, and SMS Gateway for Disaster Early Warning System, *Indonesian Journal of Geography*, Vol. 50, No. 1, 70–77. doi:10.22146/ijg.17574.

25. Meju, M. A., and Le, L. (2002). Geoelectromagneticexploration For Natural Resources:Models, Case Studies and Challenges, *Surveys in Geophysics*, Vol. 23, 133–205.

26. Lange, D., Tilmann, F., Henstock, T., Rietbrock, A., Natawidjaja, D., and Kopp, H. (2018). Structure of the Central Sumatran Subduction Zone Revealed by Local Earthquake Travel-Time Tomography Using an Amphibious Network, *Solid Earth*, Vol. 9, No. 4, 1035–1049. doi:10.5194/se-9-1035-2018.

27. Lin, J. Y., Sibuet, J. C., Hsu, S. K., and Wu, W. N. (2014). Could a Sumatra-like Megathrust Earthquake Occur in the South Ryukyu Subduction Zone?, *Earth, Planets and Space*, Vol. 66, No. 1, 1–8. doi:10.1186/1880-5981-66-49.

28. Siringoringo, L. P., Sapiie, B., Rudyawan, A., and Sucipta, I. G. B. E. (2024). Origin of High Heat Flow in the Back-Arc Basins of Sumatra: An Opportunity for Geothermal Energy Development, *Energy Geoscience*, Vol. 5, No. 3, 100289. doi:10.1016/j.engeos.2024.100289.

29. Hochstein, M. P., and Sudarman, S. (1993). Geothermal Resources of Sumatra, *Geothermics*, Vol. 22, No. 3, 181–200. doi:10.1016/0375-6505(93)90042-L.